

## Chapter 3

# Design, Analysis, and Fabrication of Quad-Ridged Horns

This chapter focuses on design and analysis of quad-ridged horns achieving near-constant beamwidth over multi-octave bandwidths. In the first section, a brief overview of the literature on dual- and quad-ridged structures is provided. The initial approach of and the software tools developed for quad-ridged horn design are detailed in the second section of the chapter. Key features of the quad-ridged horn and its design are discussed in detail. In addition, quad-ridged horn fabrication details are briefly reviewed. The chapter concludes with an outline of the method used to compute aperture mode content of the QRFH.

### 3.1 Historical Overview

Dual-ridged waveguides have been identified for their ultra-wideband capabilities as early as the 1940s [36, 37]. Most of the initial analyses relied on transverse-resonance methods and on deriving equivalent circuits for the ridged waveguide to calculate cutoff frequencies. Hopfer [38] expanded upon the existing literature by providing parametric studies of cutoff frequencies, attenuation, etc. Montgomery [39] generalized the analysis to include the complete eigenvalue spectrum of these structures. These studies all showed that the dual-ridged waveguide exhibits significantly larger bandwidth compared with hollow waveguides due to the ridges lowering the dominant mode cutoff frequency by nearly a factor of four. The term “bandwidth” is defined here as the ratio of cutoff frequency of the dominant mode to that of the next higher-order mode, i.e., single-mode bandwidth. The major practical limitation of dual-ridged waveguides and horns is the fact that they can only support single linear polarization; hence, quad-ridged structures, initially thought to also support similarly large bandwidths, gained prominence where dual linear polarization was required.

Quad-ridged waveguides have been analyzed using the finite-element method [40] and magnetic field integral equations [41, 42] for cutoff frequencies and mode fields of the first few modes as a

function of ridge-to-ridge gap and ridge thickness. These analyses show that while the dominant mode cutoff frequency in quad-ridged structures is also decreased by nearly factor of four, the single-mode bandwidth of such waveguides is not as large as their dual-ridged counterparts. This is due to mode splitting of the  $TE_{21}$  and  $TE_{20}$  modes of circular and square waveguides, respectively, whereby cutoff frequency of one of the split modes is significantly loaded by the ridges causing it to decrease along with the dominant mode. Despite having reduced single-mode bandwidth, quad-ridged structures are still widely used in many microwave applications requiring octave to multi-octave bandwidths, e.g., wideband ortho-mode transducers (OMTs) [43, 44], quad-ridged horns [45, 46, 47]. This is due to two reasons: 1) many applications do not require single mode propagation; 2) if structure has both  $x$ - and  $y$ - symmetry (two-fold symmetry), the  $TE_{21}$  ( $TE_{20}$ ) mode will not be excited.

Design of quad-ridged waveguide structures—especially ones with flared cross sections in the direction of propagation—still suffer from lack of a theoretical or empirical analysis. The aforementioned papers on quad-ridged waveguides only address the first few eigenmodes whereas more knowledge on the eigenvalue spectrum of the structure and the coupling between eigenmodes via tapered ridges/walls are needed to efficiently design components such as the horns presented herein. In the absence of such relationships, design and development of these components have traditionally been based on numerical analysis.

## 3.2 Numerical Design Approach

While desired aperture mode coefficients can be computed in a relatively straight-forward fashion as explained in the previous chapter, finding the geometry to realize the necessary aperture modes is difficult and can only be done by trial and error numerical design. Numerical electromagnetic analysis of antennas spanning multi-octave bandwidths, on the other hand, usually requires long simulation times. In order to accelerate this process and facilitate unattended operation, an extensive software setup was established early in this research. A number of scripts were written in MATLAB to communicate with the electromagnetic solver CST Microwave Studio (MWS) [48] via Matlab's COM and CST's Visual Basic interfaces, in addition to performing computations such as those in Chapter 2. Figure 3.1 shows a flow diagram of the optimization algorithm.

The quad-ridged horn geometry is represented in MATLAB by approximately 15 parameters, the most important of which are shown in Figure 3.2. The first step in the optimization is to provide the initial set of parameters defining the QRFH geometry, the frequency range of interest, and the subtended angle to the primary (secondary) reflector. While not shown in the flow chart of Figure 3.1, the user also selects at this point the subset of parameters to be used in the optimization routine and defines a range for each such that the optimization is carried out within this range.

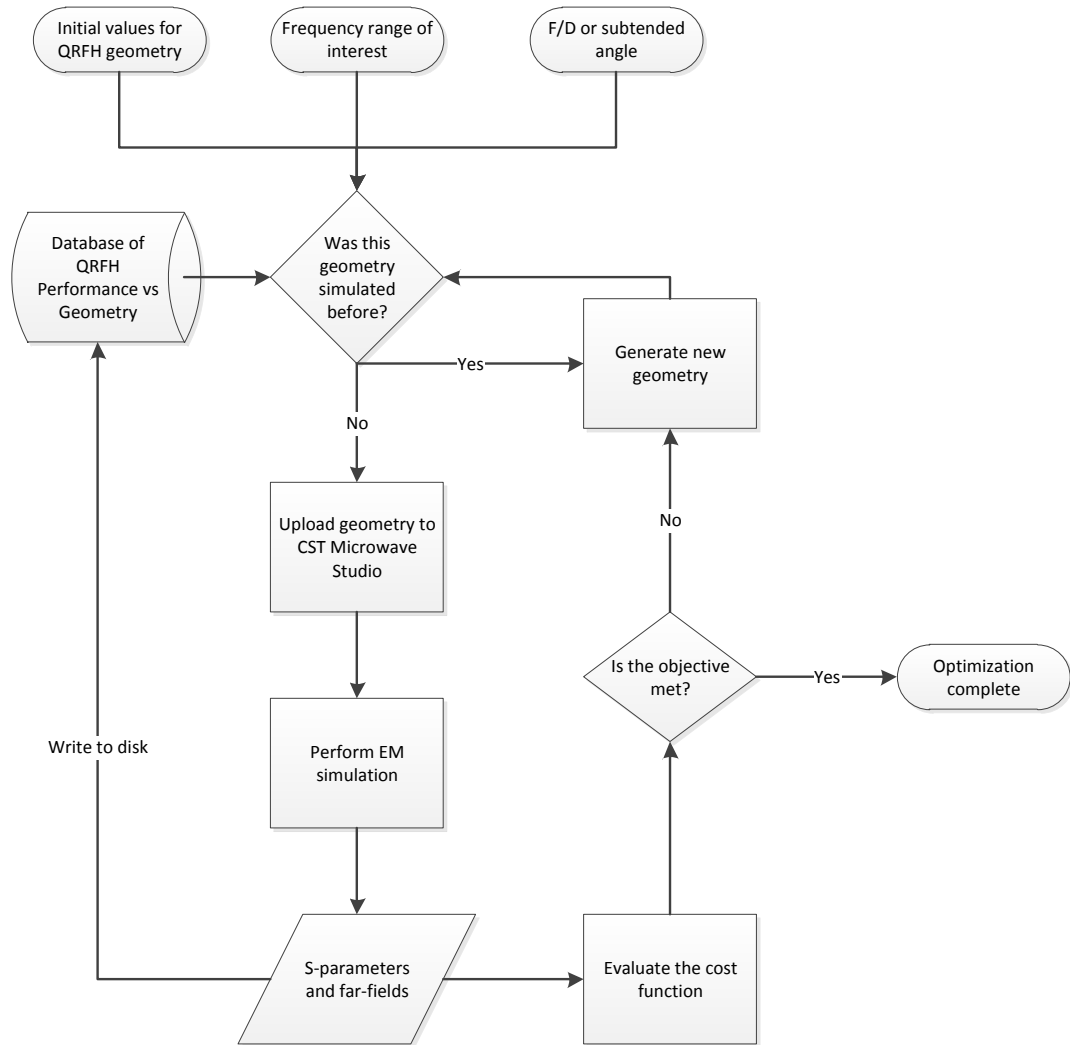


Figure 3.1: The optimization algorithm used for QRFH design. All the steps except “Perform EM simulation” are executed in MATLAB.

The software then checks the existing database to ensure the initial QRFH geometry input by the user has not been simulated previously. If the geometry has been simulated previously, a new set of parameters are generated so that each simulated geometry is unique. Once a unique parameter set is found, the geometry is uploaded to CST MWS and the EM simulation is started. Upon completion of the simulation, MATLAB commands CST to write scattering parameters and far-field patterns to disk for archiving.

The data set is also simultaneously read into MATLAB to calculate the optimization cost function. The cost function involves the input reflection coefficient, aperture efficiency, and ratio of power in the main beam of a  $\cos^q$  pattern of a given edge taper to that of the simulated patterns. The input reflection coefficient error is represented by three terms. First, define the return loss and standing-wave ratio errors as, respectively,

$$\Gamma_{err}(f_i) = 20 \log_{10} |\Gamma_{sim}(f_i)| + 10 \quad (3.1)$$

$$SWR_{err}(f_i) = SWR_{sim}(f_i) - 2 \quad (3.2)$$

where  $\Gamma_{sim}(f_i)$  and  $SWR_{sim}(f_i)$  are, respectively, the simulated reflection coefficient and standing-wave ratio as a function of discrete frequency  $f_i$ ; and the +10 and -2 terms on the right-hand sides are because the return loss optimization goal is  $\geq 10$  dB (equivalent to  $SWR \approx 2$ ). These errors are stored in vector format in MATLAB and all the negative error terms are discarded. Then, the three terms in the cost function proportional to the reflection coefficient are

$$\Gamma_{err-mean} = \frac{1}{N} \sum_{i=1}^N \Gamma_{err}(f_i) \quad (3.3)$$

$$\Gamma_{err-max} = \max[\Gamma_{err}(f_i)] \quad (3.4)$$

$$\mathbf{SWR}_{err} = SWR_{err}(f_i) \text{ for } i = 1, \dots, M \quad (3.5)$$

where the index  $M$  is usually much less than  $N$ , the total number of frequency points at which the scattering parameters are calculated. The point of this last term is to increase error weights at the low-frequency end of the QRFH band, which is where the QRFH becomes close to cutoff and return loss rapidly approaches 0 dB ( $\Rightarrow SWR \rightarrow \infty$ ). The aperture efficiency is calculated per the equations in Section 2.2 and the aperture efficiency error is given as

$$\boldsymbol{\eta}_{err}(f_i) = 55\% - 100 \times \eta_{sim}(f_i) \quad (3.6)$$

where  $\eta_{sim}$  is calculated as described in Section 2.2 and discrete frequency  $f_i$  represents the frequencies at which the radiation patterns are calculated (usually much fewer than number of frequency points used in scattering parameter simulation). The final error term in the cost function compares

the simulated radiation patterns to the ideal  $\cos^q$  pattern in the  $E$ - and  $H$ -planes. The user defines the desired edge taper,  $ET$ , at the half subtended angle  $\theta_s$  and from this, the  $\cos^q$  pattern is easily obtained

$$g(\theta) = \cos^q \theta \text{ with } q = \frac{ET}{20 \log_{10}(\cos \theta_s)}. \quad (3.7)$$

This pattern is then integrated to get the “total power” and compared with the integral of the simulated patterns in the  $E$ - and  $H$ -planes, namely

$$\mathbf{PWR}_{\text{err-E}} = \frac{\int_0^{\frac{\pi}{2}} E_{sim}(\theta) |_{\phi=0^\circ} \sin \theta d\theta}{\int_0^{\frac{\pi}{2}} g(\theta) \sin \theta d\theta} \quad (3.8)$$

$$\mathbf{PWR}_{\text{err-H}} = \frac{\int_0^{\frac{\pi}{2}} E_{sim}(\theta) |_{\phi=90^\circ} \sin \theta d\theta}{\int_0^{\frac{\pi}{2}} g(\theta) \sin \theta d\theta} \quad (3.9)$$

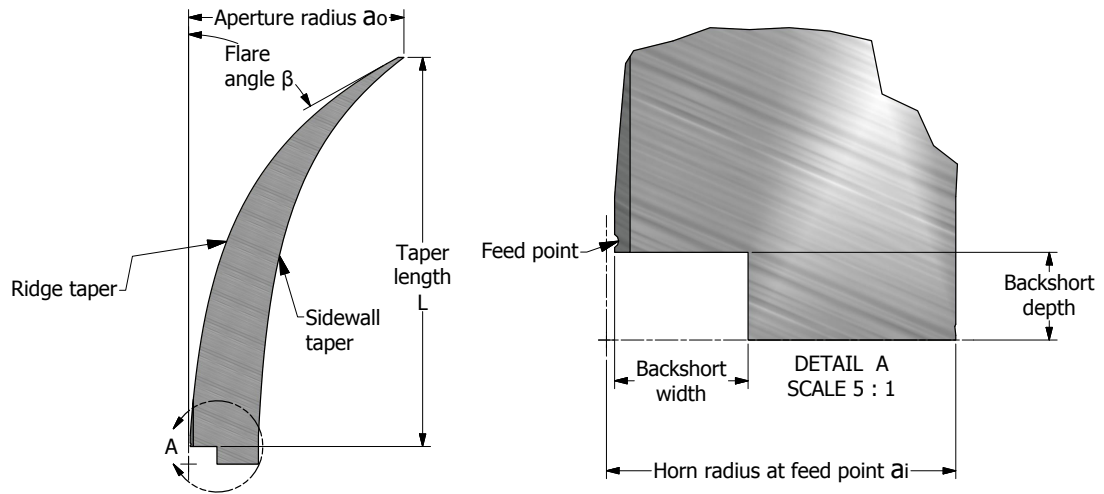
The purpose of these terms is to ensure that not only the simulated edge taper approaches the desired value, but also to avoid nulls and large ripples in the main beam. The final cost vector is then given by

$$C = \begin{bmatrix} \Gamma_{err-mean} \\ \Gamma_{err-max} \\ \mathbf{SWR}_{\text{err}} \\ \eta_{\text{err}} \\ \mathbf{PWR}_{\text{err-E}} \\ \mathbf{PWR}_{\text{err-H}} \end{bmatrix}$$

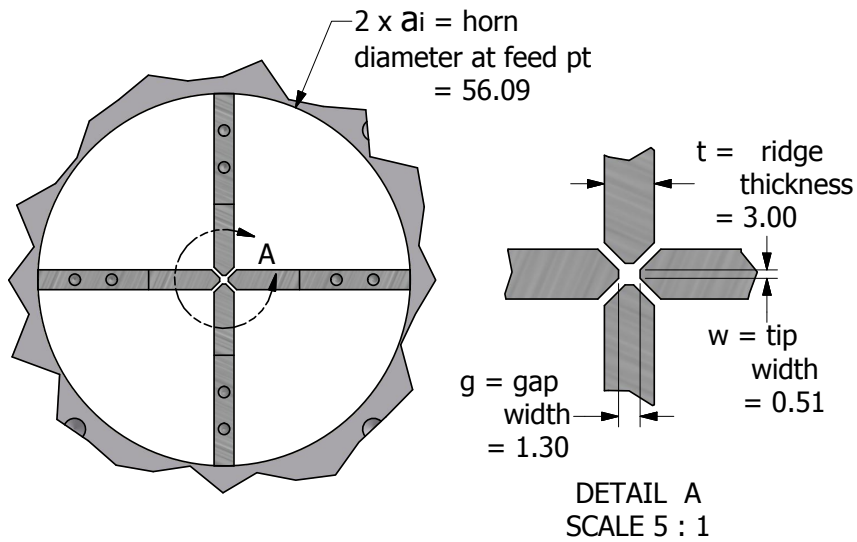
where bold-face indicates vector quantities dependent on frequency. Once the cost function is evaluated, MATLAB resumes the optimization until design objectives are met.

Three built-in MATLAB optimization routines have been used in this research, namely `lsqnonlin`, `GlobalSearch`, `simulannealbnd`. The first is the default non-linear least-squares optimizer in MATLAB. It has the advantage of estimating Jacobian of the cost function with respect to the optimization variables thereby learning to predict how a given change in one parameter will affect the cost function. Its biggest disadvantage, however, is that it can easily converge to and get stuck in a local minima, which severely limited its use in this research. The last two routines are part of Matlab’s global optimization toolbox. The most time was spent using the simulated annealing algorithm. Its rate of convergence is very slow; however, it automatically restarts the optimizer with a randomly generated parameter set after a prescribed number of iterations. This results in better coverage of the parameter space and has yielded the most number of useful QRFH geometries.

This automated software configuration, combined with a dedicated workstation with a graphics processing unit (GPU), has enabled tremendous decrease in simulation times and facilitated compilation of an extensive database of quad-ridged horn performance as a function of geometric parameters



(a)



(b)

Figure 3.2: (a) Ridge side view, (b) view from the bottom looking up. Dimensions in (b) are in millimeters and are the actual dimensions of the first QRFH built. Coordinates of the ridge and horn profiles of this QRFH (the medium gain QRFH) are provided in Appendix A

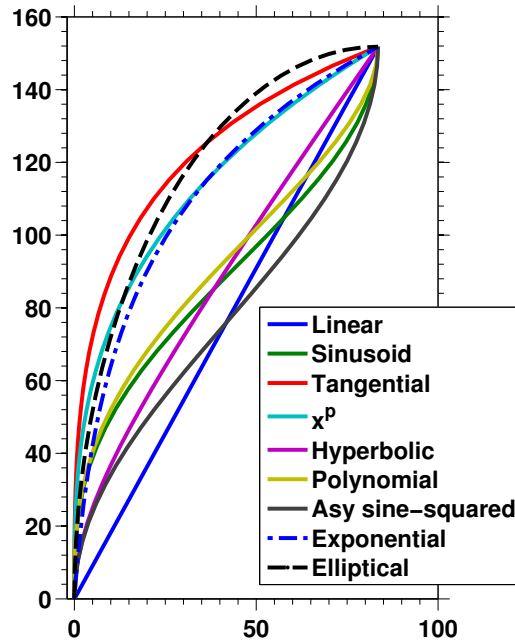


Figure 3.3: Plots of the profiles listed in Table 3.1.

(with more than 15000 different geometrical configurations and counting). While such an extensive database is costly in terms of storage space, the archived results are frequently re-evaluated using different criteria, cost functions, etc., serving as excellent baselines for new QRFH designs.

### 3.3 The QRFH Design: A Qualitative Look

While there are many parameters defining the quadruple-ridge horn geometry, designing a quad-ridge horn with a prescribed beamwidth reduces to proper selection of the ridge and sidewall profiles. The optimal ridge/wall profile combination is the one that achieves:

1. Circular radiation pattern with the desired 10 dB beamwidth over the frequency range of interest, and
2. Smooth impedance transformation between 50 Ohm and free-space impedance.

While majority of the prior work on double- and quadruple-ridged horns focuses on exponential and elliptical profiles for both ridges and sidewall, we have investigated many other profiles in this research, most of which are from corrugated and smooth-wall horn literature [49]. Expressions for all the profiles used in this work and their plots for a typical QRFH geometry are presented in Table 3.1 and Figure 3.3, respectively.

As explained in Section 3.5, obtaining constant beamwidth from a circular aperture necessitates an aperture field distribution that shrinks in area as frequency is increased (see Figure 3.7(a))

Profile name	Expression
Linear	$a(z) = a_i + (a_o - a_i) \frac{z}{L}$
Sinusoid	$a(z) = a_i + (a_o - a_i) \left[ (1 - A) \frac{z}{L} + A \sin^p \left( \frac{\pi z}{2L} \right) \right]$
Tangential	$a(z) = a_i + (a_o - a_i) \left[ (1 - A) \frac{z}{L} + A \tan^p \left( \frac{\pi z}{4L} \right) \right]$
$x^p$	$a(z) = a_i + (a_o - a_i) \left[ (1 - A) \frac{z}{L} + A \left( \frac{z}{L} \right)^p \right]$
Hyperbolic	$a(z) = \sqrt{a_i^2 + \frac{z^2(a_o^2 - a_i^2)}{L^2}}$
Polynomial	$a(z) = a_i + (p+1)(a_o - a_i) \left( 1 - \frac{pz}{(p+1)L} \right) \left( \frac{z}{L} \right)^p$
Asymmetric sine-squared	$a(z) = \begin{cases} a_i + \frac{2(a_o - a_i)}{1+\gamma} \sin^2 \left( \frac{\pi z}{4L_1} \right) & 0 \leq z \leq L_1 \\ a_i + \frac{2(a_o - a_i)}{1+\gamma} \left[ \gamma \sin^2 \left( \frac{\pi(z+L_2-L_1)}{4L_2} \right) + \frac{1-\gamma}{2} \right] & L_1 \leq z \leq L \end{cases}$ where $L = L_1 + L_2$ and $\gamma = \frac{L_2}{L_1}$
Exponential	$a(z) = (1 - A) \left[ a_i + (a_o - a_i) \frac{z}{L} \right] + A \left( c_1 e^{Rz} + c_2 \right)$ where $c_1 = \frac{a_o - a_i}{e^{RL} - 1}$ , $c_2 = \frac{a_i e^{RL} - a_o}{e^{RL} - 1}$ .
Elliptical	$x = a_o + r_1 \cos \theta \cos \phi - r_2 \sin \theta \sin \phi$ $z = r_1 \cos \theta \sin \phi + r_2 \sin \theta \sin \phi$ where $r_1 = \max(a_o, L)$ , $r_2 = \min(a_o, L)$ , $\phi = \begin{cases} 0, & a_o > L \\ \pi/2, & \text{else} \end{cases}$

Table 3.1: Profile options considered in this work. All profiles except the exponential and elliptical are from [49]; the exponential profile is a modified version of the one in [50].  $a_i$  and  $a_o$  are the radii at the feed point and horn aperture, respectively;  $L$  is the taper length;  $R$  is the exponential opening rate;  $p$  is the exponent of sinusoid, polynomial,  $x^p$ , and  $\tan^p$  profiles and can take on values in the range  $[0, \infty]$ ;  $A$  is a parameter between  $[0, 1]$  that determines how much linear taper is added.

assuming uniform phase at the aperture. Figure 3.4(a) presents  $|E_x|$  (left) and  $\angle E_x$  (right) at the aperture of the first QRFH at 1, 2, 3.5, 5, and 6  $f_{lo}$ . It is immediately observed that the aperture field magnitude distribution in the horizontal plane (plane of the excited polarization) is quite constant over the 6:1 frequency range (field distribution in the vertical plane shows more variability). In contrast,  $|E_x|$  and  $\angle E_x$  of an identical horn but without the ridges display significant variability both in terms of amplitude and phase distributions as shown in Figure 3.4(b).

Figure 3.4(a) reveals that in the case of the quad-ridge horn, it is the aperture area with uniform phase that is shrinking as frequency is increased. This is attained predominantly by the ridge profile. Specifically, difference in path lengths along the horn's longitudinal axis and along the ridge profile introduces additional phase to fields near the aperture rim. The additional phase accrued increases as frequency is increased which results in the reduced aperture area with uniform phase. This is very similar to smooth-wall and corrugated horns which are sometimes referred to as flare-angle limited horns. The flare angle for the QRFH geometry is defined in Figure 3.2(a) and primarily determines the beamwidth of the horn in  $\phi = 0^\circ$  and  $45^\circ$  planes. To illustrate this point, two sets of simulations are carried out which use the design of the first built QRFH (see Section 4.4) as baseline. This quad-ridge horn employs exponential ridge and sidewall tapers with the functional form given in Table 3.1.

In the first case, the exponential opening rate,  $R$  of Table 3.1, is varied  $\pm 40\%$  with respect to the as-built value of  $R_0$ , thereby changing the flare angle. Fig. 3.5(a) shows the simulated ridge profiles with all other parameters fixed. 10 dB beamwidths in  $\phi = 0, 45, 90$  degree planes at a constant frequency of 5 GHz are plotted in Fig. 3.5(c). Strong dependence of beamwidth on flare angle is noted in the  $\phi = 0, 45$  degree planes.  $H$ -plane beamwidth shows markedly weaker dependence.

For the second set of simulations, aperture diameter of the quad-ridge horn is swept from  $-20\%$  to  $+40\%$  of the as-built value,  $D_0$ , while maintaining identical flare angles, which requires scaling of horn's taper length. Resulting profiles are depicted in Fig. 3.5(b) and Fig. 3.5(d) plots 10 dB beamwidths and lowest useable frequency which show that aperture size has only a secondary effect on both.

While the flare angle—or more generally, the ridge profile—determines the nominal beamwidth of the horn, the ridges serve another important purpose. Namely, they enable multi-octave-bandwidth operation by lowering cutoff frequency of the dominant waveguide mode. The parameters defining the geometry near the bottom of the horn, shown in 3.2(b), are critical for achieving such wideband operation, and are:

1. horn radius at the throat;
2. ridge-to-ridge gap width  $g$ ;
3. ridge thickness  $t$ ;

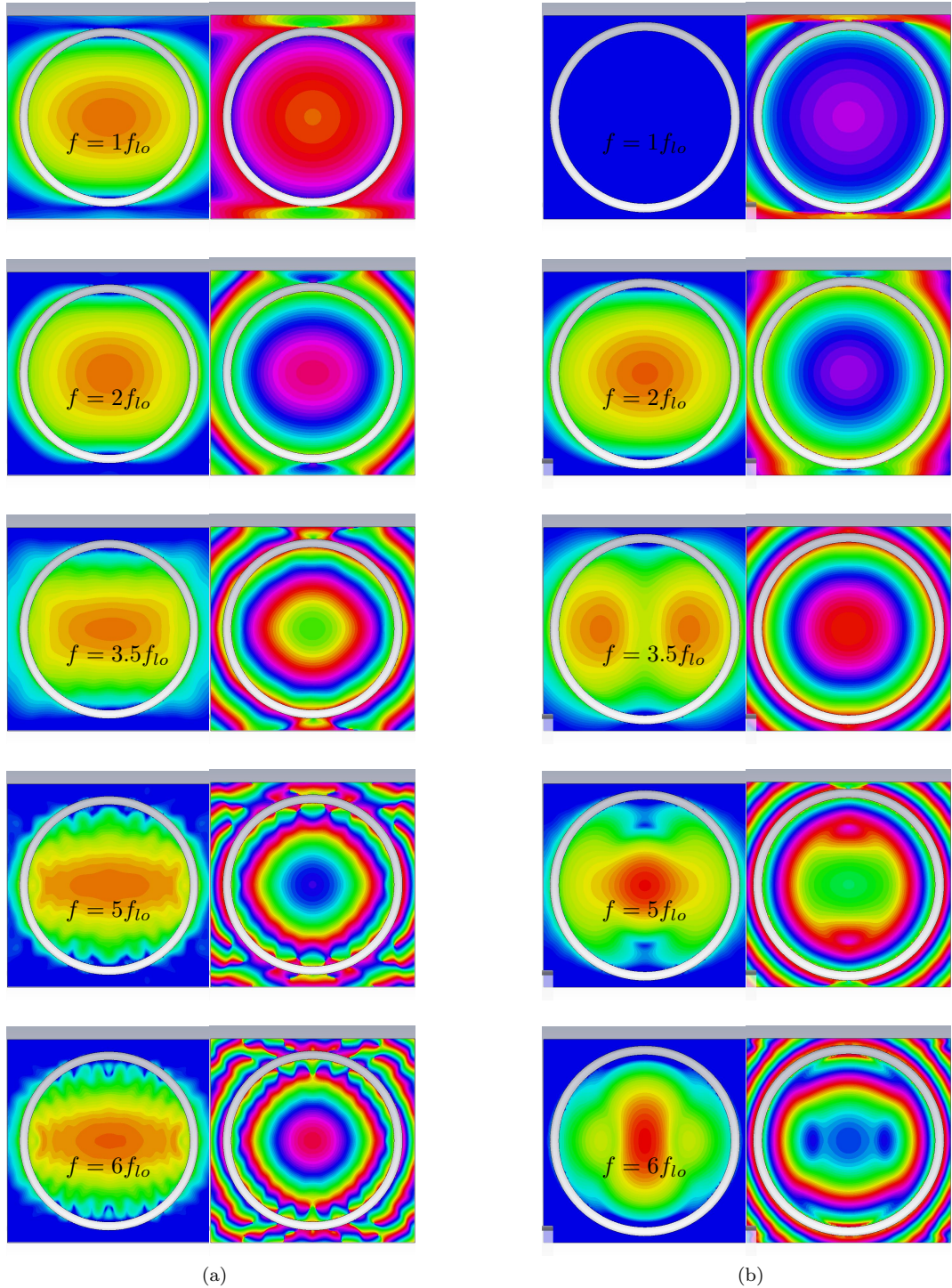


Figure 3.4:  $x$ -directed aperture fields of (a) the medium gain QRFH of Section 4.4, (b) identical horn but without the ridges. Magnitude is plotted on the left and phase on the right for both (a) and (b). All plots are on the same scale.

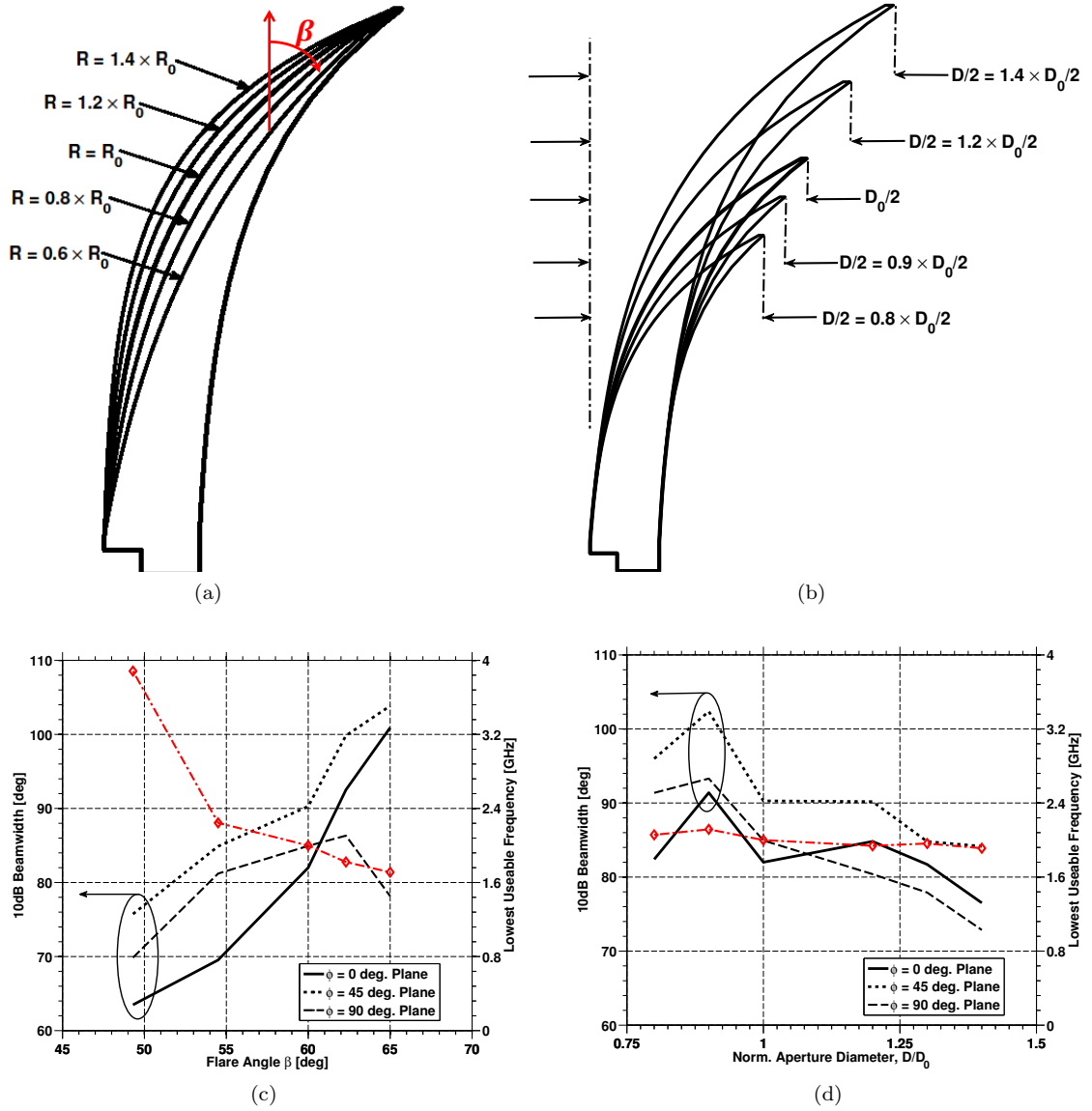


Figure 3.5: Side view of the ridge as: (a) exponential opening rate is swept from -40% to +40% of the baseline value  $R_0$ , (b) aperture diameter is swept from -20% to +40% of the baseline value  $D_0$ ; 10 dB beamwidth in  $\phi = 0, 45, 90$  degree planes (at a constant frequency of 5 GHz) and lowest useable frequency as a function of: (c) the exponential opening rate of the ridge, (d) the aperture diameter.  $\phi = 0, 45, 90$  curves are plotted using, respectively, solid, dash-dotted and dashed lines. Dash-dotted curve with diamond markers is lowest useable frequency below which the quad-ridge horn is cutoff. The flare angle  $\beta$  is shown in part (a).

#### 4. ridge tip width $w$

where the last three are not independent. As shown in [42], heavily loaded ridges, namely  $g \rightarrow 0$ , lower cutoff frequency of the dominant mode by as much as factor of four. For example, cutoff frequency of the dominant mode in a circular waveguide of radius 27.395 millimeters (as-built radius of the medium gain QRFH of Section 4.4) is 3.21 GHz whereas the cutoff frequency of the dominant mode in the same waveguide but with heavily loaded ridges is computed numerically to be 0.85 GHz. Comparing the top plots in Figure 3.4(a) and (b) also underline this fact, which show that in the absence of the ridges, the horn is below cutoff at 2 GHz. Increasing ridge thickness also reduces the dominant mode cutoff frequency, but its impact is much less pronounced.

Another consideration in selecting the ridge and sidewall profiles is that the ridge-to-ridge gap must be small enough at any cross section along the horn's longitudinal axis to ensure propagation of the dominant mode in the desired frequency range. The dominant mode cutoff frequency is a strong function of gap width implying the cutoff frequency increase due to a small increase in the gap width can only be offset by a larger change in the sidewall radius. This, in turn, makes the horn prone to unwanted higher-order mode excitation. For example, the lowest useable frequency of Figure 3.5(c) does not approach the cutoff frequency in the throat, namely 0.85 GHz, because the dominant mode is below cutoff further up in the horn due to ridge-to-ridge gap increasing rapidly. In summary, horn radius at the throat, gap width  $g$  and the ridge profile are critical in determining the lowest useable frequency of the horn.

The gap width, in conjunction with the ridge thickness, also establishes the nominal input impedance of the horn. Smaller gap width translates to lower input impedance and vice versa. Same effect can also be obtained by increasing the ridge thickness. This suggests that not only tip-to-tip gap width is critical but also the gap between adjacent ridges (along the chamfered edges) which, to a large extent, is controlled by the gap width. This is because thicker ridges—or smaller gap width—implies larger shunt capacitance.

### 3.4 Fabrication Considerations

The quad-ridge horns built to date have been built in pieces using a numerically controlled milling machine. The base of the horn (i.e. around the feed point) is the most critical part in terms of tolerances on dimensions, locations and orientations of the ridges. The gap width and ridge-to-ridge distance along the chamfered edges (see Figure 3.2(b)) are the primary factors determining input impedance, and proper location and orientation of ridges are of utmost importance to avoid unwanted higher-order mode excitations due to asymmetry.

The feed point of the QRFH is inherently asymmetric due to different diameter holes in two opposing ridges; however, this asymmetry is very minor and does not excite higher-order modes.

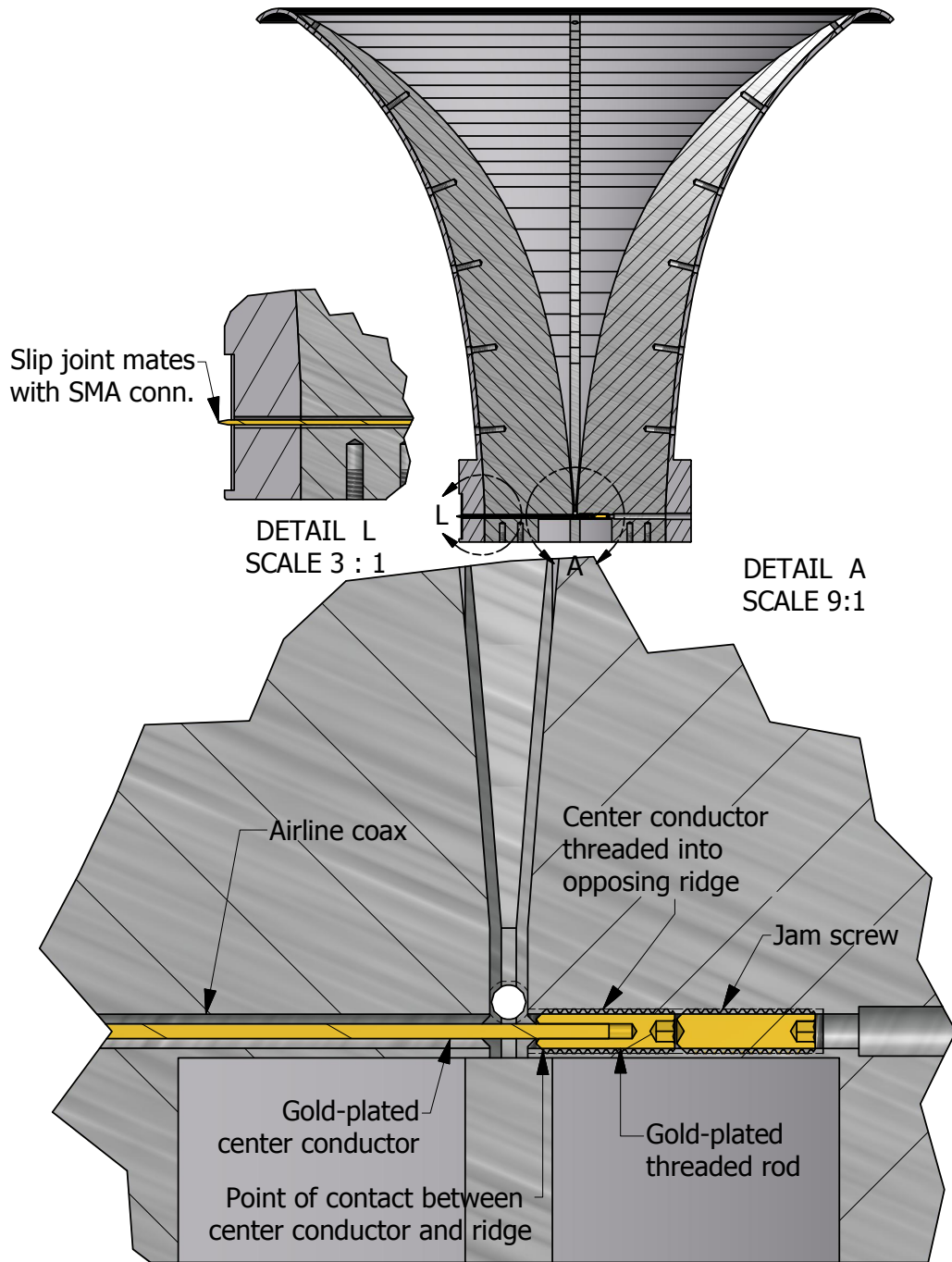


Figure 3.6: Detailed view of input coax center conductor connection with opposing ridge. The other two ridges and sidewall are not shown in Detail A for clarity.

If, on the other hand, the ridge location and orientation is not properly set, it would have a direct impact on the mode content due to the changing boundary conditions in the horn.

While numerically controlled parts facilitate keeping of tolerances, the fact that ridges are bolted onto the sidewall and difficulty of drilling ridge mounting holes at precise locations suggest that another method be used to constrain the ridge orientation and location. Two mounting holes per ridge on the flat bottom plate and guiding pins are used to keep the ridges at the proper locations. Ridge-to-sidewall as well as ridge-to-backplate mounting holes are shown in Figure 3.6.

A low-loss coaxial air line through one ridge with center conductor connected to the opposite ridge is used to form a balun and excite the ridge waveguide at the base of the horn. The connection of the center conductor of this air line to the opposite ridge is quite critical. This could be accomplished with a pin socket for the center conductor but a more positive contact was selected which also allows some adjustment of the contact point. An accurate 0.508 mm diameter gold-plated gage pin is press-fit into a short 0-80 threaded stud which screws into a threaded hole through the opposite ridge. A set screw from the back of the ridge is then utilized to lock the thread of the center conductor. The input end of the center conductor plugs into a well-formed socket of a commercial SMA connector with a slip joint to accommodate tolerances and differential thermal expansion of center conductor and horn body. A small degree of tuning of the feed return loss is accomplished by turning the threaded rod to adjust the contact point in the opposite ridge. These details are provided in the bottom half of Figure 3.6. It is also worth noting that because coaxial line of the second polarization is physically above the first one, there is inherently a slight performance difference between two ports.

### 3.5 Aperture Mode Content

Before proceeding to example QRFH designs of the next chapter, a method for calculating  $TE$  and  $TM$  mode coefficients required at a circular aperture to achieve given radiation patterns is presented. This procedure is based on [29] and is used in the next chapter to evaluate aperture mode content of the quad-ridged horns.

The approach relies on the fact that far-field patterns of all hollow circular waveguide modes are expressed in closed form [29, 51]. Neglecting reflections at the aperture, the far-field patterns of transverse-electric mode  $TE_{mn}$  are

$$E_{\theta,mn}^{TE} = -a_{mn} j^m m J_m(X'_{mn}) \frac{J_m(ka \sin \theta)}{ka \sin \theta} \cos m\phi \Psi(\theta) \quad (3.10)$$

$$E_{\phi,mn}^{TE} = a_{mn} j^m X_{mn}'^2 J_m(X'_{mn}) \frac{J_m'(ka \sin \theta)}{X_{mn}'^2 - (ka \sin \theta)^2} \sin m\phi \Psi(\theta) \quad (3.11)$$

and those of the transverse-magnetic mode  $TM_{mn}$  are

$$E_{\theta, mn}^{TM} = b_{mn} j^m X_{mn} J'_m(X_{mn}) \frac{ka \sin \theta J_m(ka \sin \theta)}{X_{mn}^2 - (ka \sin \theta)^2} \cos m\phi \Psi(\theta) \quad (3.12)$$

where

$$\Psi(\theta) = \frac{ka^2}{2} (1 + \cos \theta) \frac{e^{-jkR}}{R}$$

$$k = \frac{2\pi}{\lambda}$$

$\lambda$  = Wavelength

$a$  = Waveguide aperture radius

$R$  = Far-field radius

$X_{mn}$  =  $n$ th zero of  $J_m(x)$

$X'_{mn}$  =  $n$ th zero of  $J'_m(x)$ ,

$m \in [0, \infty]$ ,  $n \in [1, \infty]$ ;  $a_{mn}$  and  $b_{mn}$  are complex amplitude coefficients of the  $TE$  and  $TM$  modes, respectively. These equations underline an important feature. Specifically,  $\phi$ -directed far-fields are determined only by the  $TE$  modes, and the shape of the  $\theta$ -directed far-fields of the  $TE$  modes depend on  $m$  but not on  $n$ . This implies that, for a given  $m$ , the  $\phi$ -component of the radiation patterns can be synthesized entirely from  $TE$  modes, and then the  $\theta$ -component may be synthesized from  $TM$  modes without affecting the former.

Consequently, an arbitrary radiation pattern  $f(\theta, \phi)$  can be written as a sum of patterns of each mode, i.e.,

$$f(u, \phi) = \frac{1 + \sqrt{1 - \left(\frac{u}{ka}\right)^2}}{2} \left\{ \sum_{\substack{m=0 \\ n=1}}^{M,N} \left[ A_{mn} \frac{mJ_m(u)}{X_{mn}^2 u} - B_{mn} \frac{uJ_m(u)}{u^2 - X_{mn}^2} \right] \cos m\phi \hat{\theta} \right. \\ \left. + \left[ A_{mn} \frac{J'_m(u)}{u^2 - X_{mn}^2} \right] \sin m\phi \hat{\phi} \right\} \quad (3.13)$$

where

$$A_{mn} = -a_{mn} j^m k J_m(X'_{mn}) X_{mn}^2 a^2$$

$$B_{mn} = b_{mn} j^m k J'_m(X_{mn}) X_{mn} a^2 \quad (3.14)$$

$$u = ka \sin \theta$$

After some algebra and using orthogonality of sine and cosine, the final expressions for the complex

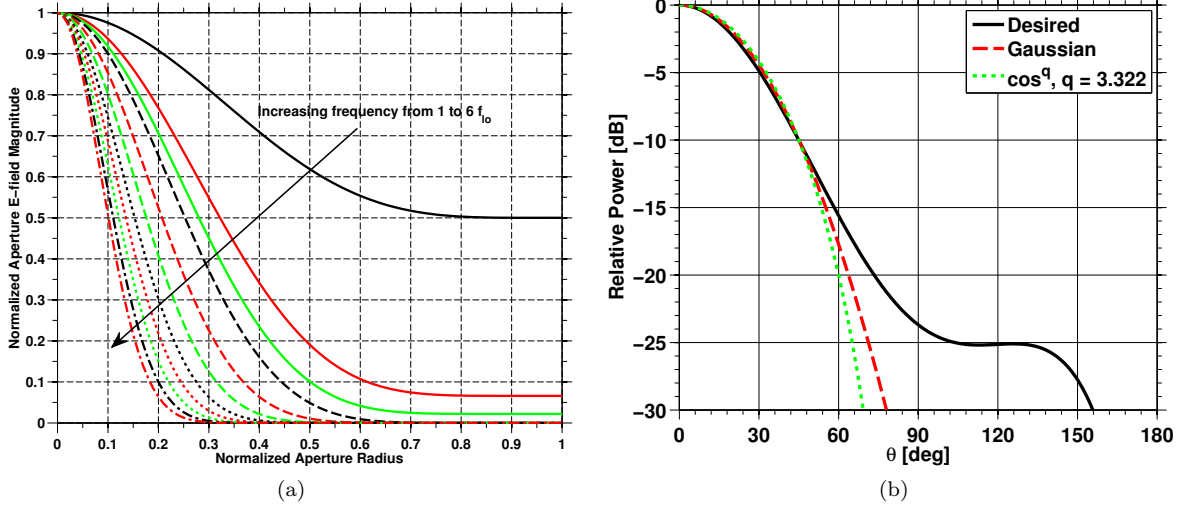


Figure 3.7: (a) Aperture distributions as a function of frequency and (b) the resultant far-field patterns (black) in addition to Gaussian (red dashed) and  $\cos^q$  (green dotted) radiation patterns. 10 dB beamwidth is 90 degrees.

mode coefficients are found to be [29]

$$A_{pq} = \frac{2}{1 + \sqrt{1 - \left(\frac{X'_{pq}}{ka}\right)^2}} \frac{2X'_{pq}}{\pi J'_p(X'_{pq})} \int_0^{2\pi} f_\phi(X'_{pq}, \phi) \sin p\phi d\phi. \quad (3.15)$$

$$B_{pq} = \frac{2}{1 + \sqrt{1 - \left(\frac{X_{pq}}{ka}\right)^2}} \frac{2}{\pi J_{p+1}(X_{pq})} \int_0^{2\pi} f_\theta(X_{pq}, \phi) \cos p\phi d\phi \quad (3.16)$$

which demonstrates that the  $TE$  and  $TM$  coefficients are in fact independent, as alluded to earlier.

Before proceeding into calculation of mode coefficients of an “ideal” radiation pattern, it is worthwhile to make a few observations. First, the summation in (3.13) is finite so long as the aperture is of finite extent and wavelength is greater than zero, because only modes above cutoff at the aperture can contribute to far-field radiation patterns, and for a given aperture size, number of such modes is always finite. Secondly, fits to the desired radiation pattern obtained through this approach are necessarily approximate, because the fitting is performed at a set of discrete points, namely  $u = X_{pq}$  for the  $\theta$ -component and  $u = X'_{pq}$  for the  $\phi$ -component.

Another important observation from these equations is that the radiation patterns of individual modes reach their maxima near the points  $u = X_{mn}$  and  $u = X'_{mn}$  for  $TM_{mn}$  and  $TE_{mn}$  modes, respectively. This implies that for a fixed aperture size, adding more modes broadens the radiation pattern. Conversely, using more modes necessitates a larger aperture to maintain constant beamwidth [29]. However, phase errors in the horn aperture can significantly degrade performance

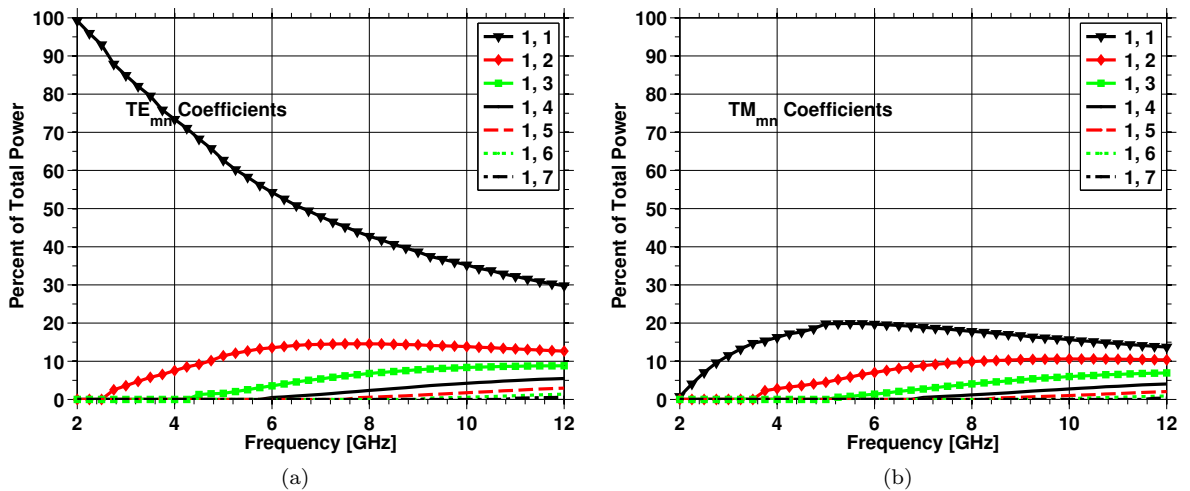


Figure 3.8: (a)  $TE$  and (b)  $TM$  modes required at a circular aperture of radius  $a = 0.6\lambda_{l_0}$  to achieve the desired far-field pattern of Figure 3.7 from 1 to 6  $f_{l_0}$ . Mode coefficients are normalized such that total power in all modes at a given frequency sums to 1.

for large apertures. This is the reason it is more difficult to design octave-band corrugated horns with wide beamwidths. The same holds for quadruple-ridged horns as demonstrated in Chapter 4.

Equations (3.15) and (3.16) are now used to calculate the necessary modes at an aperture with radius  $0.6\lambda_{l_0}$  to achieve circularly symmetric radiation pattern with 10 dB beamwidth of 90 degrees. Figure 3.7(a) shows the aperture distributions required to achieve far-field patterns with 90 degree beamwidth over 6:1 frequency band which are calculated using the results in [27, 52]. The far-field pattern obtained from these distributions are plotted in part (b) of the same figure in black along with Gaussian and  $\cos^q$  patterns yielding the same beamwidth.

The mode coefficient computations are performed in MATLAB [53] and the results are provided graphically in Figure 3.8. A subset of the results are also listed in Table 3.2. As expected, the  $TE_{11}$  mode is the dominant mode throughout the frequency range; however, its relative power decreases monotonically with frequency. The next three most significant modes are  $TM_{11}$ ,  $TE_{12}$ , and  $TM_{12}$ . This observation, as well as the relative power content in each mode, is in good agreement with the power distribution in an optimum four-mode horn [29].

The requirement of circular symmetry in the radiation patterns necessitates far-field patterns exhibiting the following azimuthal dependence<sup>1</sup>

$$f(u, \phi) \propto V_\theta(u) \cos \phi \hat{\theta} + V_\phi(u) \sin \phi \hat{\phi}. \quad (3.17)$$

As observed from (3.13), such patterns are attained with only  $m = 1$  modes at the aperture. The results of Figure 3.8, where only  $m = 1$  modes are present, confirm this point. Lack of even-order

<sup>1</sup>This is the “optimum” far-field pattern of Ludwig [29].

Mode	Frequency			
	$1f_{l_0}$	$3f_{l_0}$	$4.5f_{l_0}$	$6f_{l_0}$
$TE_{11}$	1.0000	1.0000	1.0000	1.0000
$TM_{11}$	0.0878	0.6027	0.6580	0.6789
$TE_{12}$	0	0.4996	0.6079	0.6517
$TM_{12}$	0	0.3605	0.5190	0.5897
$TE_{13}$	0	0.2556	0.4480	0.5440
$TM_{13}$	0	0.1595	0.3645	0.4828
$TE_{14}$	0	0.0949	0.2941	0.4289
$TM_{14}$	0	0	0.2248	0.3687
$TE_{15}$	0	0	0.1693	0.3155
$TM_{15}$	0	0	0.1209	0.2619
$TE_{16}$	0	0	0	0.2159
$TM_{16}$	0	0	0	0.1728
$TE_{17}$	0	0	0	0.1372
$TM_{17}$	0	0	0	0.1058

Table 3.2: Amplitudes of  $TE$  and  $TM$  modes, normalized to that of  $TE_{11}$ , required to realize the desired radiation pattern of Figure 3.7 with a circular aperture of radius  $a = 0.6\lambda_{l_0}$ . All modes are in phase with  $TE_{11}$ .

modes, e.g.  $m = 0, 2, 4, \dots$ , is due to perfect two-fold symmetry of the aperture field distribution. Moreover, the curves in this figure reinforce the earlier point on the need to have more modes at the aperture to maintain large beamwidth and circular beam as aperture size grows in terms of wavelength.

We conclude this section by highlighting the inherent assumptions in the above development. One of these assumptions, neglecting reflections at the aperture, has already been mentioned. More importantly, this development also approximates the guide wavelength at the aperture with the free-space wavelength. This is certainly not true for the example calculation presented in Figure 3.8 at the low end of the frequency band where, for instance, the aperture diameter is only  $1.2\lambda_{l_0}$ . On the other hand, it is a fairly good assumption in the upper half of the frequency band for the first three or four modes. It is possible to address both of these assumptions by modifying equations (3.10-3.12) as outlined in [51]. This, however, is not pursued, because the increase in accuracy gained from such an exercise is thought to be small, especially when the aperture mode calculation is applied to circular quadruple-ridged horns as is done in Chapter 4.